nature portfolio

https://doi.org/10.1038/s41586-025-09612-9

Supplementary information

Global warming amplifies wildfire health burden and reshapes inequality

In the format provided by the authors and unedited

Supplementary information for:

Global warming amplifies wildfire health burden and reshapes inequality

Junri Zhao[1], Bo Zheng[1,2*], Philippe Ciais[3], Yang Chen[4], Thomas Gasser[5,3], Josep G. Canadell[6], Longyi Zhang[1], Qiang Zhang[7*]

[1]Shenzhen Key Laboratory of Ecological Remediation and Carbon Sequestration, Institute of Environment and Ecology, Tsinghua Shenzhen International Graduate School, Tsinghua University, Shenzhen 518055, China.

[2]State Environmental Protection Key Laboratory of Sources and Control of Air Pollution Complex, Beijing 100084, China.

[3]Laboratoire des Sciences du Climat et de l'Environnement, LSCE/IPSL, CEA-CNRS-UVSQ, Université Paris-Saclay, Gif-sur-Yvette, France.

[4]Department of Earth System Science, University of California, Irvine, Irvine, CA 92697, USA.

[5]International Institute for Applied Systems Analysis (IIASA), Schlossplatz 1, 2361 Laxenburg, Austria.

[6]CSIRO Environment, Canberra, ACT 2601, Australia.

[7]Ministry of Education Key Laboratory for Earth System Modeling, Department of Earth System Science, Tsinghua University, Beijing, China

**Correspondence to*: Bo Zheng (bozheng@sz.tsinghua.edu.cn) and Qiang Zhang (qiangzhang@tsinghua.edu.cn)

Content of this file:

Supplementary Note 1: ML framework for global burned area estimates

We trained the XGBoost[1] (machine learning algorithm under the Gradient Boosting framework) model to capture the nonlinear relationships between burned area (BA) and multiple climate factors that strongly affect fire occurrence[2,3], and further estimate the global BA. Hyperparameter optimization is a crucial step in improving ML model performance. In this study, the GridSearchCV tool in Scikit-learn (https://scikitlearn.org/stable/modules/generated/sklearn.model_selection.GridSearchCV.html) was used for hyperparameter tuning, which includes both grid search and cross-validation. In the grid search, all parameter combinations within a specified range were explored by adjusting the parameters with a specified step size to train the learning algorithm. Cross-validation is a statistical analysis method used to verify the performance and generalization ability of algorithm classifiers. Finally, we chose the set of hyperparameters that yielded the highest average coefficient of determination (i.e., the R^2 regression score function) across all validation sets.

The input data for the ML model consist of BA from Global Fire Emissions Database, Version 4.1 (GFED4.1s) [4], and climate data, including 2 m air temperature (T2), relative humidity (RH), total precipitation (TP), 10m wind speed (W10), leaf area index (LAI), evaporation from the top of canopy (Evaporation). These climate data are sourced from the monthly estimates of four Earth system models (ESMs) and the European Centre for Medium-Range Weather Forecasts Reanalysis version 5 (ERA-5) dataset[5]. Furthermore, to account for seasonal climate variations and the spatiotemporal heterogeneity of climate factors on fire occurrences, we incorporated the sampling times (Time) and geographic coordinates (Coordinate) of the input data into the ML framework. To address data discontinuity, these datasets were transformed into periodic functions, following methods recommended in previous studies[6-8]:

$$\left[\frac{\mathrm{M1}}{\mathrm{M1}}\right] = \left[\frac{\cos\left(\mathrm{month}\,\frac{2\pi}{12}\right)}{\sin\left(\mathrm{month}\,\frac{2\pi}{12}\right)}\right] \tag{1}$$

$$\begin{bmatrix} L1 \\ L2 \\ L3 \end{bmatrix} = \begin{bmatrix} \sin\left(\text{lat}\frac{\pi}{180}\right) \\ \sin\left(\text{lat}\frac{\pi}{180}\right)\cos(lat\frac{\pi}{180}) \\ -\cos\left(\text{lon}\frac{\pi}{180}\right)\cos(lat\frac{\pi}{180}) \end{bmatrix} \tag{2}$$

The terms month, lat, and lon refer to the sampling data's month, latitude, and longitude, respectively, while M1-M2 and L1-L3 denote the resulting calculations of periodic functions.

Due to large fluctuations in the input data, we applied log transformation and normalization to reduce variability. The dynamic range of predictors was constrained to the [−1,1] interval using min–max normalization, as recommended in prior research[9]:

$$Y_{norm} = \left[\frac{Y\text{-}Y_{min}}{Y_{max}\text{-}Y_{min}}\right] \tag{3}$$

where Y_{min} and Y_{max} are the minimum and maximum values in the data Y, respectively.

The transformed input data were matched to the BA data, which were aggregated into global monthly data on a 2°×2.5° grid. To evaluate the predictive performance of the ML model, we conducted annual out-of-sample predictions for historical data from 2000–2014. For example, to predict 2014 BA, we used data from 2000–2013 for training; for 2013 BA, data from 2000–2012 and 2014 were used, and so on. Detailed evaluation results are provided in Supplementary Note 2. For future projections (2015–2099), we trained the ML model on historical data and employed ESM-projected future climate factors for prediction.

Supplementary Note 2: Evaluation of BA and fire emissions from 2000 to 2014

To validate the application of the fitted relationship in the projection of future changes in wildfire emissions, we conducted a performance assessment by comparing the ML predictions of BA with the satellite-derived burned area used in the GFED4.1s framework for the period 2000 to 2014. The results demonstrate that our predictions (PRD (BA)) successfully reproduced the observed declining trend of BA (−6.4 Mha yr^{-2}) both temporally (Extended Data Fig. 1(a)) and spatially (Supplementary Figs. 1(a,c)), showing a similar rate of −6.0 (−6.2 to −5.8) Mha yr^{-2}.

The mean annual PRD (BA) of 466.6 (453.8 to 477.0) Mha yr^{-1} was slightly lower than the mean value of GFEDv4.1s (BA) (475.7 Mha yr^{-1}) for the same period (2000–2014). This discrepancy likely stems from the model's underestimation in fire-prone regions of Africa and Australia (Supplementary Figs. 1 (b,d)). To evaluate model performance across regions, we compared our results with the GFEDv4.1s using GFED's global region partitions[10] (Supplementary Fig. 6). The comparison (Supplementary Fig. 2) shows strong agreement, with Pearson's R^2 values ranging from 0.72 to 0.96. However, overall predictions slightly underestimate, with slopes generally ranging from 0.8 to 0.9. The Africa region—where global wildfire activity is most concentrated—shows particularly good performance, with both slope and R^2 values aligning well.

However, the ESMs are known to have inherent biases[11] that may impact predictive performance. To further evaluate the accuracy of the ML model driven by ESMs' climate factors, we employed data from ERA-5 to estimate global burned areas (PRD (BA, ERA5)). Our findings indicate that both PRD (BA) and PRD (BA, ERA5) exhibit minor differences in the spatial distribution of BA trends (Supplementary Figs. 1(c,e)) and biases in BA (Supplementary Figs. 1(d,f)) compared to GFEDv4.1s. Both models capture the monthly temporal variations in global mean BA (Supplementary Fig. 7), which suggests that the predictive performance of both models remains relatively consistent. The ML model was trained and applied using meteorological data from ESMs with internally consistent projections. ERA-5 reanalysis data were used only for independent evaluation and not as input predictors. To avoid discontinuities between historical and future periods, we used a single, continuous set of climate forcings from

ESMs for both ML training and projection. While this strategy may introduce model-specific biases, a parallel experiment driven by ERA5 forcings shows modest deviations, indicating that our main conclusions are not sensitive to the forcing choice. The ML model determines the relative weights of the four ESM inputs alone.

Then, in order to assess the simulation performance of ESMs regarding fire emissions, we conducted a recalculation of global fire carbon emissions using PRD (BA) with GFEDv4.1s fuel, applying the equation: burned area × fuel consumption × emission factor. Extended Data Figs. 1(b-d) provide a comparative analysis between global fire carbon emissions derived from GFEDv4.1s and those simulated by ESMs and PRD (BA)-based global fire carbon emissions for the period 2000–2014. A notable mean bias is observed in the magnitude (0.9 Pg yr^{-1}) and spatial pattern of fire carbon emissions simulated by ESMs when compared to satellite observation-based estimates (GFEDv4.1s (C)). However, our estimates (PRD (C)) substantially mitigate this bias, demonstrating improvements in both the magnitude bias (-0.2 Pg yr^{-1}) and spatial pattern of fire carbon emissions when compared to GFEDv4.1s (C). The bias in our prediction results for global fire carbon emissions aligns with those reported in other studies[3,12], which range from −0.3 to 0.2 Pg yr^{-1}. Our findings suggest that ESMs may overestimate fire emissions, while our ML framework, incorporating satellite-based burned area data, provides more accurate constraints on global and regional scales.

Supplementary Note 3: Projected trends in BA and vegetation biomass in response to future climate change

ML-based projections of future BA under the SSP2-4.5 scenario show a gradual decline, whereas under the SSP5-8.5 scenario, BA demonstrates an overall increasing trend (Supplementary Fig. 3(a)), in contrast to the historical BA trend. Supplementary Figs. 3(c, e) illustrate that sub-Saharan Africa exhibits a decreasing BA trend in future scenarios, resembling the historical trend (Supplementary Fig. 1). However, in most regions outside of sub-Saharan Africa, BA shows an increasing trend, particularly prominent under the SSP5-8.5 scenario, which offsets the declining trend in sub-Saharan Africa and results in a global upward BA trend in the SSP5-8.5 scenario.

Regarding the simulation of vegetation biomass by ESMs, both future scenarios show an increasing trend in high-latitude regions of the Northern Hemisphere, the Amazon region, and other areas (Supplementary Figs. 3(d, f)). This increase is likely attributable to projected warming and the CO_2 fertilization effect[13], leading to enhanced biomass production and accumulation. It is noteworthy that both BA and biomass exhibit an increasing trend in high-latitude regions of the Northern Hemisphere in future scenarios (Supplementary Fig. 3). The observed trend of increasing vegetation biomass and burned area in high-latitude regions of the Northern Hemisphere under future scenarios have implications for changes in fire emissions and the geographical redistribution of fire-prone regions, with a potential shift towards northern latitudes.

Supplementary Note 4: Driver analysis of global BA projection

In this research, we employed the SHapley Additive exPlanation (SHAP)[14] method to assess the importance of each predictor in the ML framework and to quantify their respective contributions. The SHAP method achieves this by constructing an additive explanation model that considers the impacts of all predictive variables on the model's output, which can be formally represented using the following equation:

$$\mathrm{y}_n = \mathrm{y}_{base} + \mathrm{f}(\mathrm{x}_{n,1}) + \mathrm{f}(\mathrm{x}_{n,2}) + \cdots + \mathrm{f}(\mathrm{x}_{n,m})$$

Here, *m* and *n* represent the feature and sample, respectively, and *base* denotes the baseline. Where y_n represents the final predicted value, y_{base} denotes the model's baseline score, which corresponds to the mean prediction across all samples for the target variable, $\mathrm{f}(\mathrm{x}_{\mathrm{n,m}})$ represents the SHAP value of the m-th feature variable for the n-th sample, indicating its impact on the target prediction.

The ultimate prediction for each sample is derived by summing the baseline score and the contribution scores from each feature variable. When $\mathrm{f}(\mathrm{x}_{\mathrm{n,m}}) > 0$, it indicates that the m-th feature variable for the n-th sample has a positive impact on the target prediction. Conversely, $\mathrm{f}(\mathrm{x}_{\mathrm{n,m}}) < 0$ suggests that the m-th feature variable for the n-th sample has a counteractive or negative impact on the target prediction. Therefore, SHAP values not only quantify the magnitude of a feature's influence on the target prediction but also express whether each feature contributes positively or negatively to the prediction. In this study, the term n-th sample refers to the predicted value of BA for a specific grid cell in a particular prediction year and month, and the term m-th feature variable refers to the climate factors as listed in Supplementary Table 2.

Eight predictors, listed in Supplementary Table 2, were evaluated for their contributions to future BA predictions using the SHAP approach. The global average importance of these predictors for BA is summarized in Supplementary Tables 4 and 5, which represent the proportion of each feature variable's 5-year mean global average absolute SHAP value relative to the cumulative SHAP values of all feature variables, The values for 2000–2014 were derived from the BA evaluation process for the historical period (Supplementary Note 2), while the values for 2015–2099 were obtained from the future projection process. Notably, the coordinate feature shows a relatively high importance, indicating its substantial influence during both training and prediction phases. Given the distinctive spatial patterns of global wildfire emissions[15], particularly the high value near the equator (10°S-10°N) and their uneven distribution across regions, we hypothesize that the ML model is more sensitive to these parameters. As discussed in Supplementary Note 1, to account for the spatiotemporal heterogeneity of climate factors and their impacts on fire occurrences, we incorporated the sampling geographic coordinates into the ML framework by transforming them into periodic functions.

Among the eight predictors, the 2m temperature (T2) demonstrated the most importance, with contribution increasing from 6.7% to 7.7% and 9.6% between 2015 and 2099 under the SSP2-4.5 and SSP5-8.5 scenarios, respectively. This suggests a growing influence of T2 in BA prediction. In Supplementary Fig. 8, the SHAP values refer to the change ratio of the 5-year mean global average SHAP value for each feature variable during 2015–2099 relative to those in 2010–2014, which presents the global average trends of each climate factor-related predictor and their contributions to BA prediction. A higher absolute SHAP value indicates a larger contribution to BA prediction compared to the preceding five years (2010–2014), while a lower SHAP value indicates a smaller contribution. For T2, the SHAP value under the SSP5-8.5 scenario initially decreases, then increases around 2060. This trend aligns with observed BA trends from 2015–2059 and 2060–2099 (Supplementary Fig. 9). In the SSP5-8.5 scenario, sub-Saharan Africa experiences a declining BA trend in both periods, while most regions outside sub-Saharan Africa show a more pronounced increase in BA from 2060–2099. This upward trend in global average BA (Supplementary Fig. 3(a)) matches the observed trend in SHAP values for T2. Therefore, this study suggests that T2 may be an important driver of future spatial and temporal trends in BA.

Several features related to drought, such as RH, Evaporation, and T2, show increasing global mean values, indicating drier trends under the SSP5-8.5 scenario (Supplementary Fig. 8, dashed curves). Correspondingly, the related SHAP values increase (Supplementary Fig. 8, solid curves), and these variations are more pronounced compared to the SSP2-4.5 scenario. This may indicate that the ML model captures the increased frequency and extent of wildfires under a future climate of global warming and increasing drought, especially under the SSP5-8.5 scenario. The increased precipitation in the SSP5-8.5 scenario, relative to SSP2-4.5, is associated with smaller predicted BA values, reflected in the decreasing SHAP values (Supplementary Fig. 8(f), solid curve). An increase in leaf area index (LAI), which reflects more available fuel, leads to larger predicted BA values (Supplementary Fig. 8(e), solid curve).

Supplementary Note 5: Model evaluation and the impact of fire emissions on global ambient $PM_{2.5}$

Fire emissions (ozone precursor gases, acidifying gases, etc) for the SSP2-4.5 and SSP5-8.5 scenarios (Supplementary Fig. 10) were reconstructed based on our projected fire carbon emissions. These emissions data, along with the GFEDv4.1s emissions data and other natural and anthropogenic emissions, were used as inputs to drive the GEOS-Chem[16] chemistry transport model with historical[17] and future[18] meteorological fields to assess the $PM_{2.5}$-related premature mortality and aerosol radiative forcing resulting from wildfire emissions during the five-year periods of 2010–2014 and 2095–2099.

Ground-based observations of $PM_{2.5}$ were obtained from four different sources: (1) hourly data for mainland China in 2014 from the China National Environmental Monitoring Center (CNEMC) (http://www.cnemc.cn/); (2) annual average data for East Asia during 2010–2014 from the Acid Deposition Monitoring Network in East Asia (EANET) (https://www.eanet.asia/); (3) 3-day average data for the United States region during 2010–2014 from the Interagency Monitoring of Protected Visual Environments (IMPROVE) (http://vista.cira.colostate.edu/Improve/); and (4) hourly data for Europe during 2010–2014 from the European Monitoring and Evaluation Programme (EMEP) (http://ebas-data.nilu.no/). Aerosol Optical Depth (AOD) ground-based observations for 2010–2014 were obtained from the AERosol RObotic NETwork (AERONET) (https://aeronet.gsfc.nasa.gov/new_web/index.html), and this study used the monthly averaged spectral deconvolution algorithm (SDA) 2.0 version[19] data to evaluate the model simulations. The original AOD observation data were obtained at 500 nm and were converted to 550 nm to allow for comparison with the model-simulated AOD, using the Ångström exponent at 500 nm. $PM_{2.5}$ and AOD observations were integrated to the GEOS-Chem (2°×2.5°) grid and compared with the corresponding simulations.

Supplementary Fig. 11 presents a comparison between the annual mean aerosol optical depth (AOD) and $PM_{2.5}$ concentrations simulated by GEOS-Chem and the observations for the period of 2010–2014. The model demonstrated a strong agreement with observations (Pearson's R=0.76 for AOD and R=0.92 for $PM_{2.5}$), with a substantial portion of the data points falling within the 1:2 and 2:1 line. The predicted $PM_{2.5}$

concentrations showed a slight underestimation, with MB values of -0.01 μg m^{-3}. This underestimation was primarily attributable to data from the year 2014 in the Chinese region (blue dots in Supplementary Fig. 11 (b)). The predicted values of AOD show a slight overestimation, as indicated by the positive MB value of 0.03.

Fire emissions resulted in average surface-level concentrations of 0.38, 0.51, and 0.65 μg m^{-3} for global $PM_{2.5}$ levels during the historical period (2010-2014) and the late 21st century (2095–2099) under the SSP2-4.5 and SSP5-8.5 scenarios, respectively (Supplementary Figs. 12(a, b, c)). Regions with high concentrations (>15 μg m^{-3}) were primarily observed in the southern hemisphere, specifically in the sub-Saharan Africa region. The global average relative contribution of fire emissions to $PM_{2.5}$ increased from 6.2% during the historical period (2010–2014) to 14.6% in the SSP5-8.5 scenario (2095–2099) (Supplementary Figs. 12(d, e, f)). More than 40% of $PM_{2.5}$ contributed by fire emissions was found in high-latitude regions of the Northern Hemisphere, where pronounced growth in fire emissions occurred (Extended Data Fig. 3 (b)).

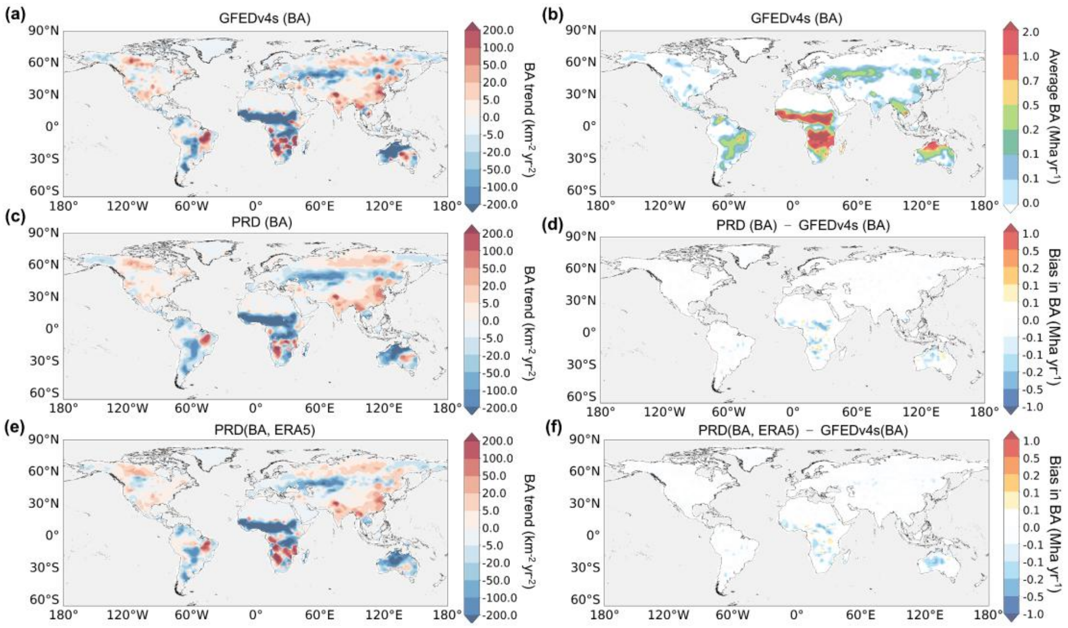

Supplementary Figure 1. Historical burned area during 2000–2014 from GFEDv4.1s and predicted in this study using an ML framework. (a) represents the trend in burned area derived from GFEDv4.1s along with those predicted in this study using climate factors from ESMs (c) and ERA5 (e). The trends in each grid cell are estimated using the linear least squares fitting method based on annual time series. The spatial distribution of annual mean burned area is shown for GFEDv4.1s (b), along with the disparities with predictions based on climate factors from ESMs (d) and ERA5 (f) compared to GFEDv4.1s.

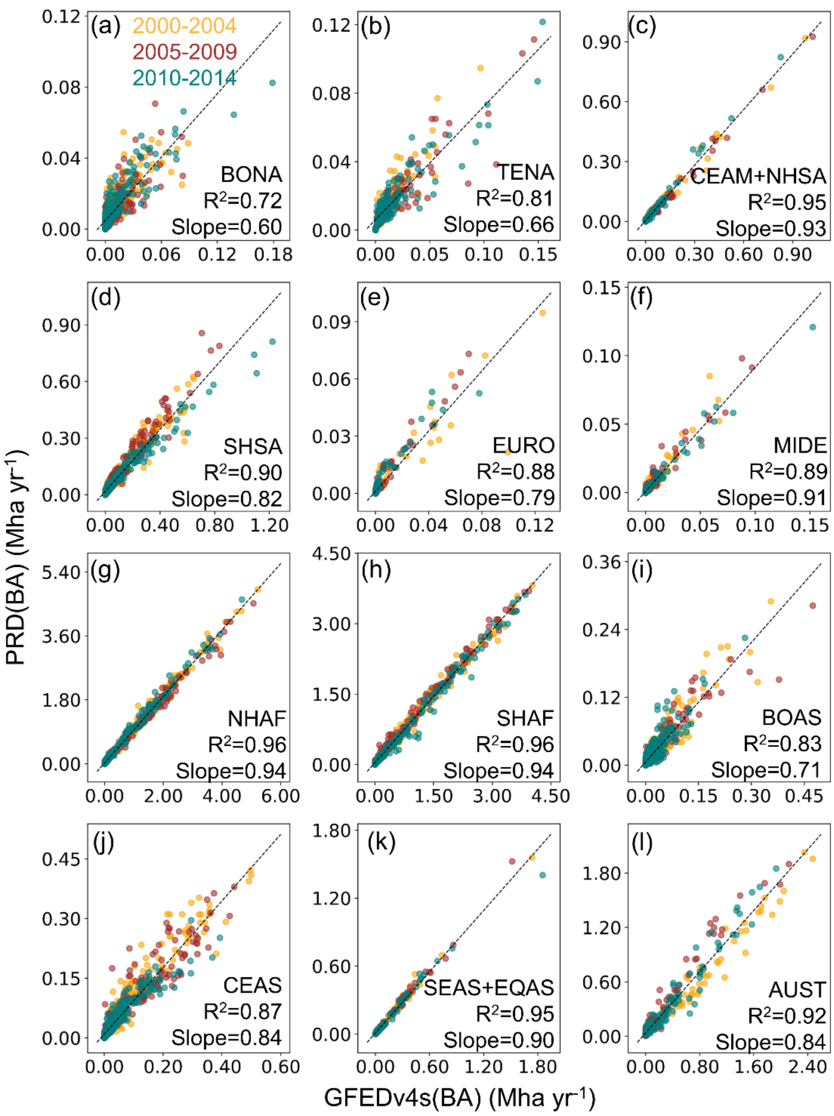

Supplementary Figure 2. Evaluation of ML-predicted burned area across different regions. Panels (a) to (l) show evaluation results for global GFED regions, with the following abbreviations: Boreal North America (BONA), Temperate North America (TENA), Central America (CEAM), Northern Hemisphere South America (NHSA), Southern Hemisphere South America (SHSA), Europe (EURO), Middle East (MIDE), Northern Hemisphere Africa (NHAF), Southern Hemisphere Africa (SHAF), Boreal Asia (BOAS), Central Asia (CEAS), Southeast Asia (SEAS), Equatorial Asia (EQAS), and Australia (AUST). The scatter plots represent 5-year average results for the periods 2000–2004, 2005–2009, and 2010–2014, as indicated in panel (a). The vertical and horizontal axis ranges vary across panels. R^2 and slope represent Pearson's correlation coefficient and the regression line slope, respectively.

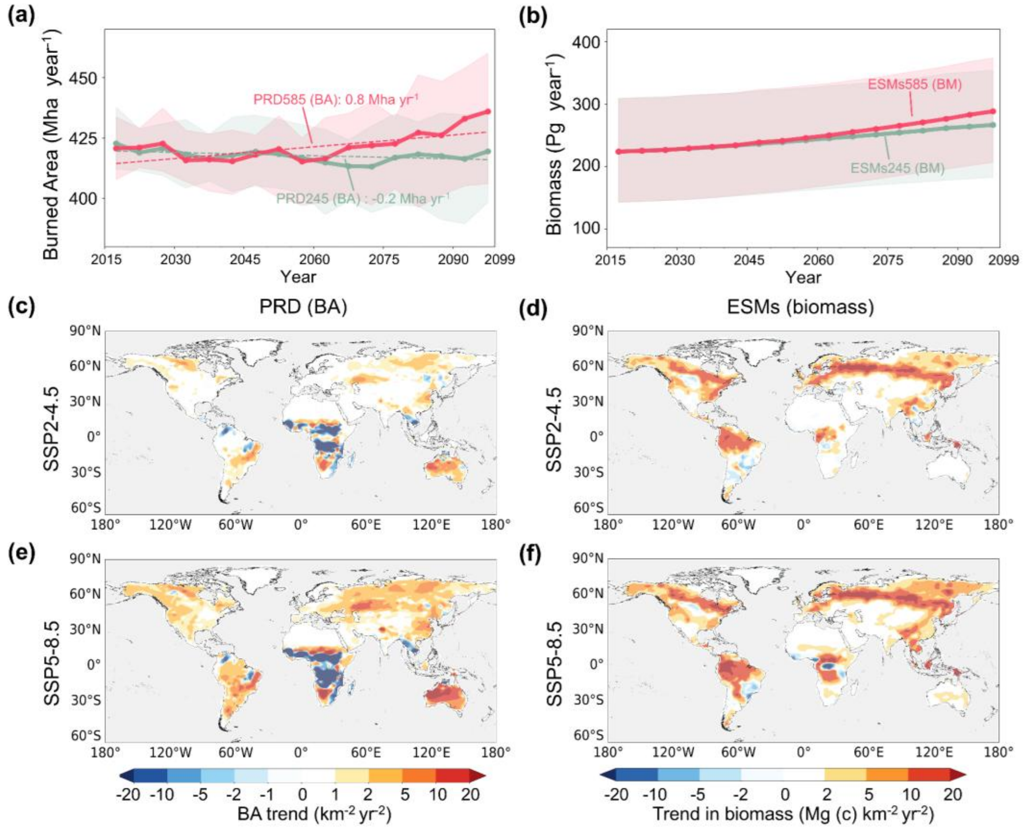

Supplementary Figure 3. Projected burned area and vegetation biomass from 2015 to 2099. (a) and (b) represent trends of global burned area in our projection and global vegetation biomass from ESMs estimates, respectively, under SSP2-4.5 (green curves) and SSP5-8.5 (red curves) scenarios. The green and red shaded areas represent the minimum and maximum ranges from estimates of four ESMs. (c) and (e) show the spatial distribution of burned area trends, (d) and (f) show the spatial distribution of vegetation biomass trends. The trends in each grid cell are estimated using the linear least squares fitting method based on annual time series.

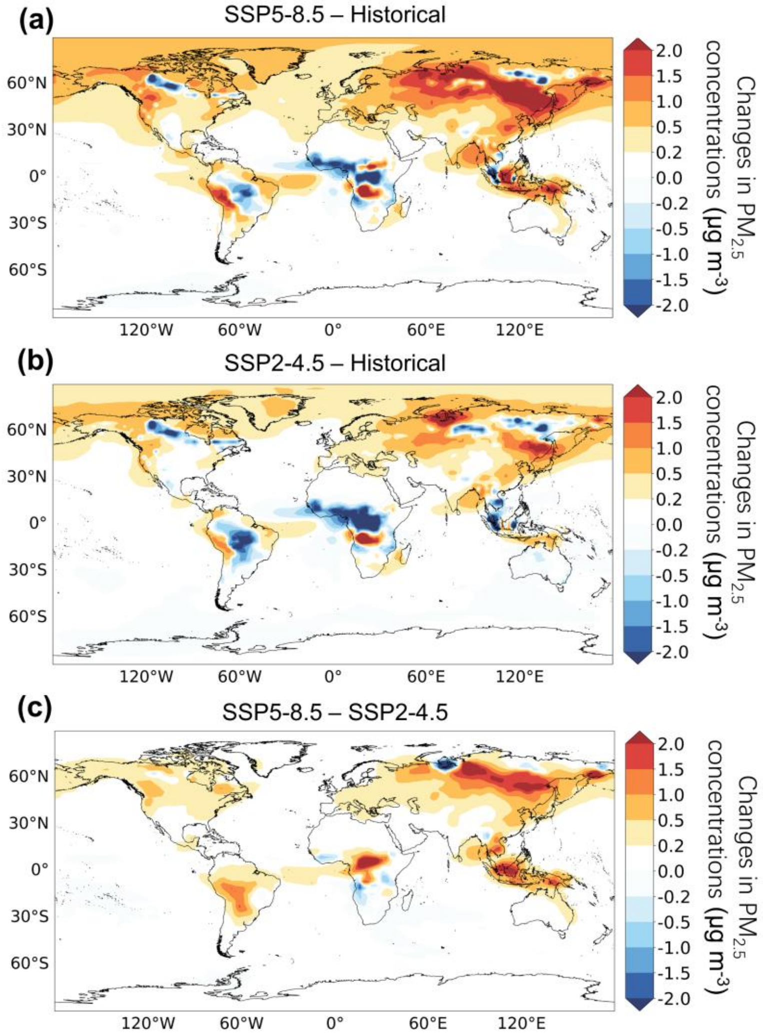

Supplementary Figure 4. Changes in surface-layer fire-induced $PM_{2.5}$ concentrations. (a) compares annual average $PM_{2.5}$ concentrations between 2095–2099 (SSP5-8.5) and 2010–2014 (the historical period). (b) shows comparisons between 2095–2099 (SSP2-4.5) and 2010–2014 (the historical period), and (c) compares SSP5-8.5 and SSP2-4.5 scenarios at 2095–2099.

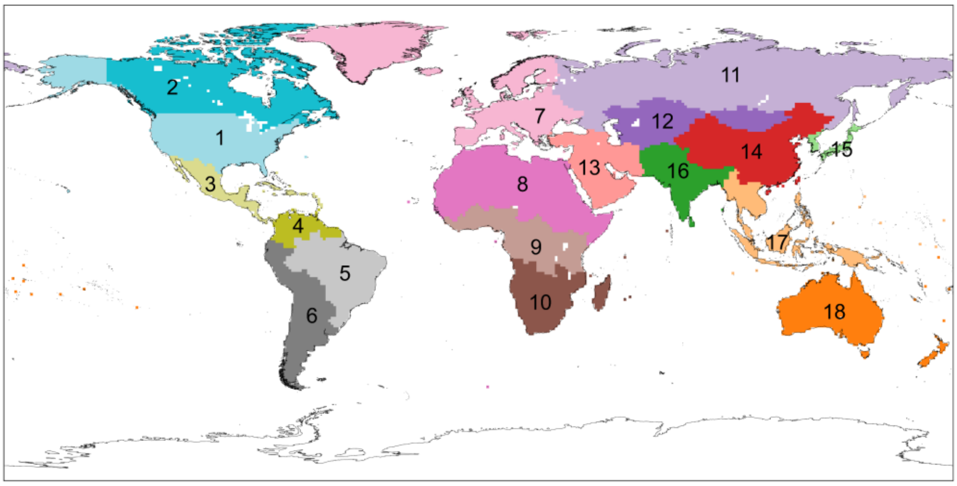

Supplementary Figure 5. Map of the 18 continental regions. 1: USA; 2: Canada; 3: Central America; 4: Northern South America; 5: Brazil; 6: Southwest Southern America; 7: Europe; 8: Northern Africa; 9: Equatorial Africa; 10: Southern Africa; 11: Russia; 12: Central Asia; 13: Middle East; 14: China; 15: Korea and Japan; 16: South Asia; 17: South East Asia; 18: Oceania. The region split data are obtained from the Saunois et al.,[20], close to the TransCom inter-comparison map[21].

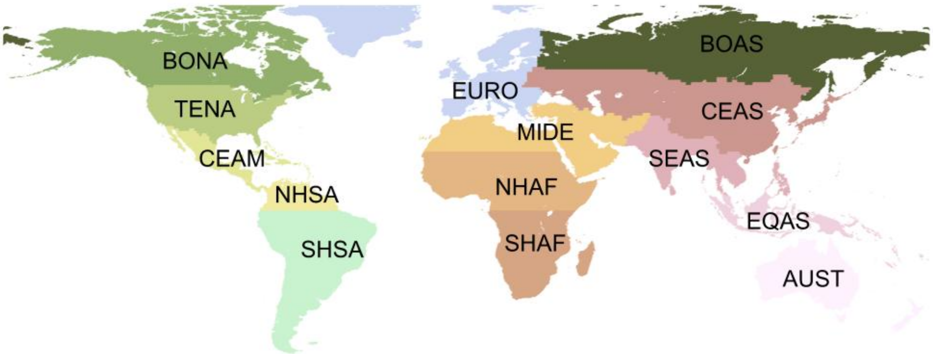

Supplementary Figure 6. The 14 region partitions used in the GFED framework[10], obtained from the publicly accessible GFEDv4.1s dataset[4].

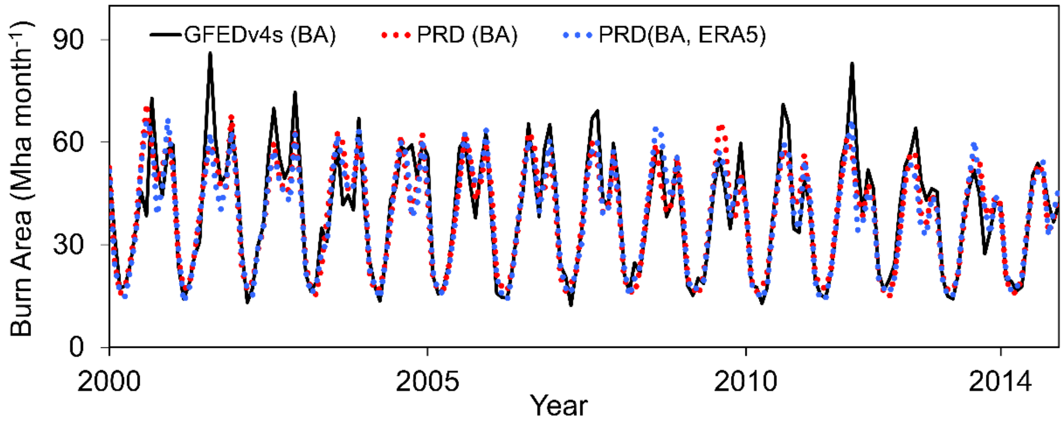

Supplementary Figure 7. Temporal trends of global monthly burned area from GFEDv4.1s (black curve) and predicted in this study using climate factors from ESMs (dashed red curve) and ERA5 (dashed blue curve) during 2000–2014.

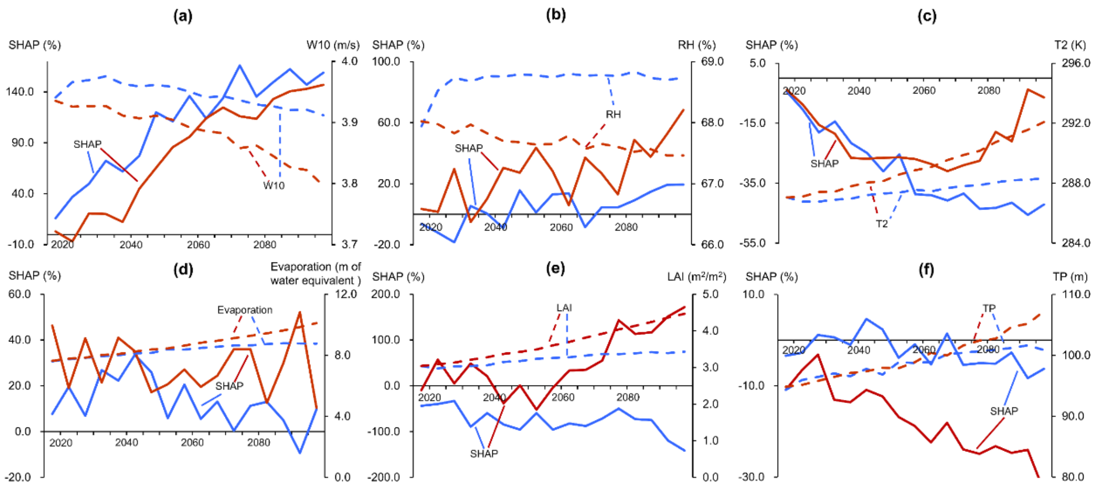

Supplementary Figure 8. The global average trends of climate factor-related predictor and their contributions to BA prediction under SSP2-4.5 (blue curves) and SSP5-8.5 (red curves) scenarios. The solid curves referred to the left-hand axis represent the change in 5-year average SHAP values from 2015 to 2099 compared to the 5-year average SHAP values from 2010 to 2014. On the right-hand axis, the dashed curves represent the global average trends of climate factors (5-year averages) over land areas.

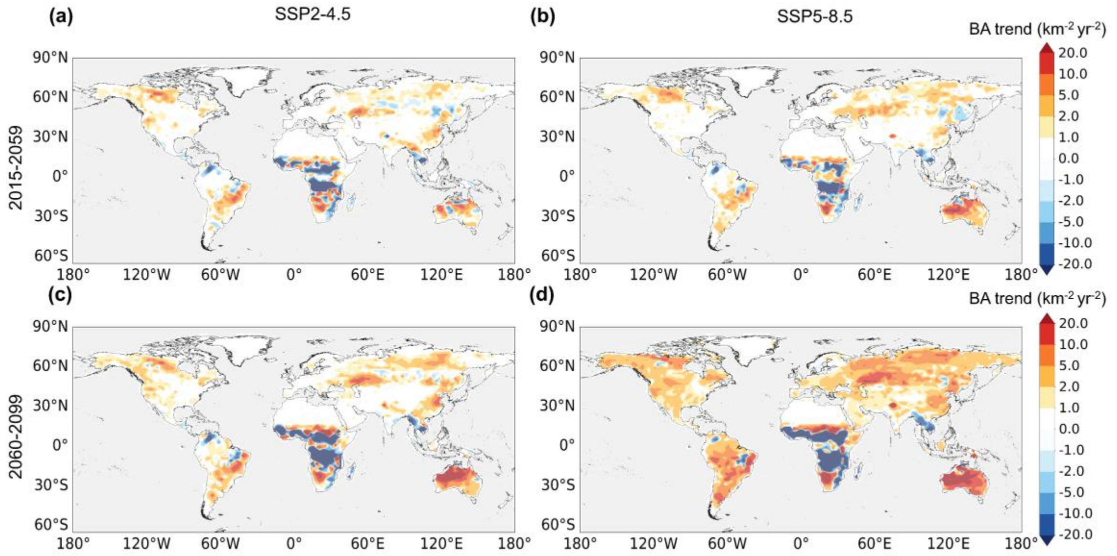

Supplementary Figure 9. Spatial distributions of burned area trends during 2015 ‒ 2059 and 2060–2099 under SSP2-4.5 and SSP5-8.5 scenarios. The left column ((a) and (c)) and right column ((b) and (d)) show trends under the SSP2-4.5 and SSP5-8.5 scenarios, respectively.

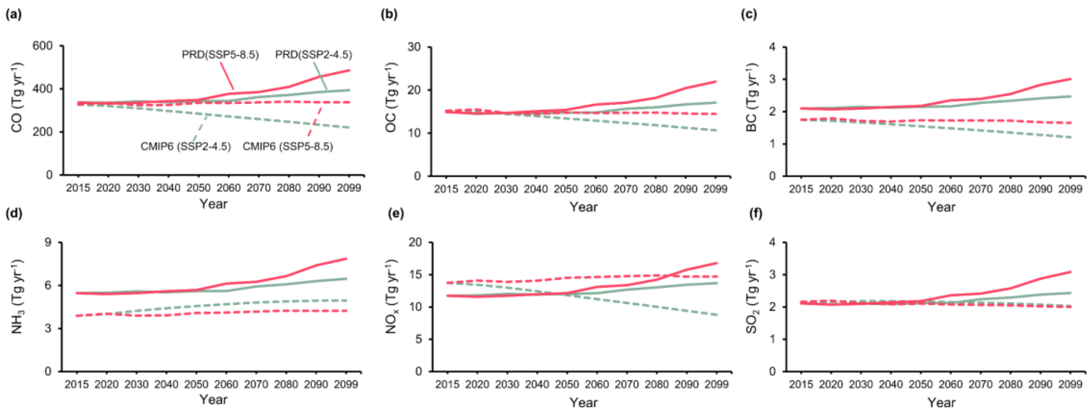

Supplementary Figure 10. Trends of global fire emissions of pollutants during 2015–2099 under SSP2-4.5 (green curves) and SSP5-8.5 (red curves) scenarios. The solid curves show the results estimated based on the fire carbon emissions prediction from our study, while the dashed curves show the fire emissions data developed for the CMIP6 experiments acquired from the Earth System Grid Federation (ESGF) (https://esgf-node.llnl.gov/projects/input4mips).

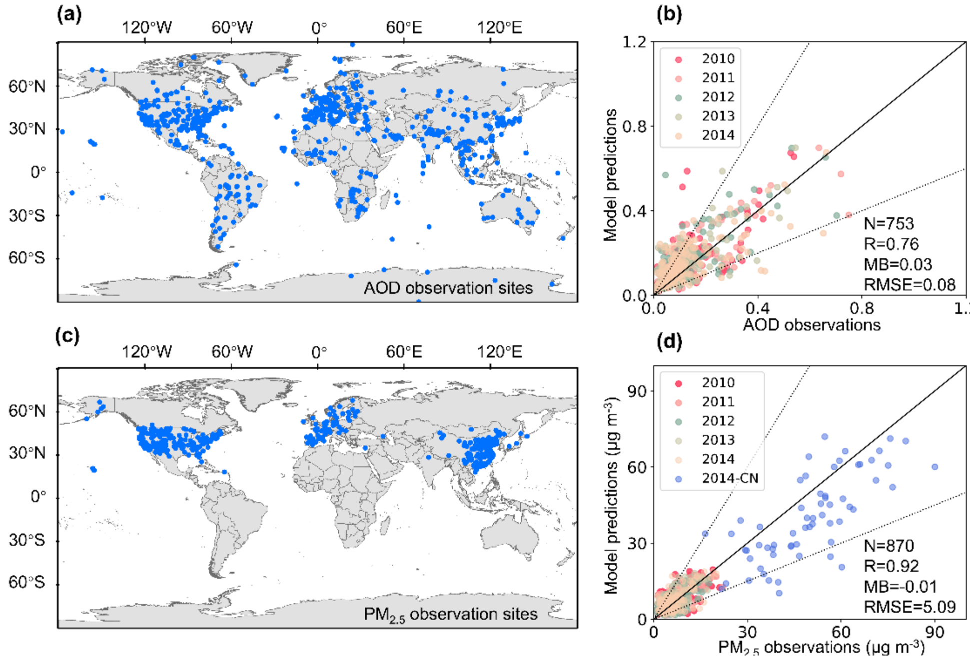

Supplementary Figure 11. Evaluation of GEOS-Chem predicted $PM_{2.5}$ and AOD against ground observations. (a) and (c) show the observation sites for AOD and $PM_{2.5}$, respectively, over the global domain during 2010 – 2014. (b) and (d) show the scatter plots of observed and GEOS-Chem predicted annual mean AOD and $PM_{2.5}$ concentrations, respectively. The black solid lines indicate the 1:1 line, and the grey dashed lines indicate the 1:2 and 2:1 relationships.

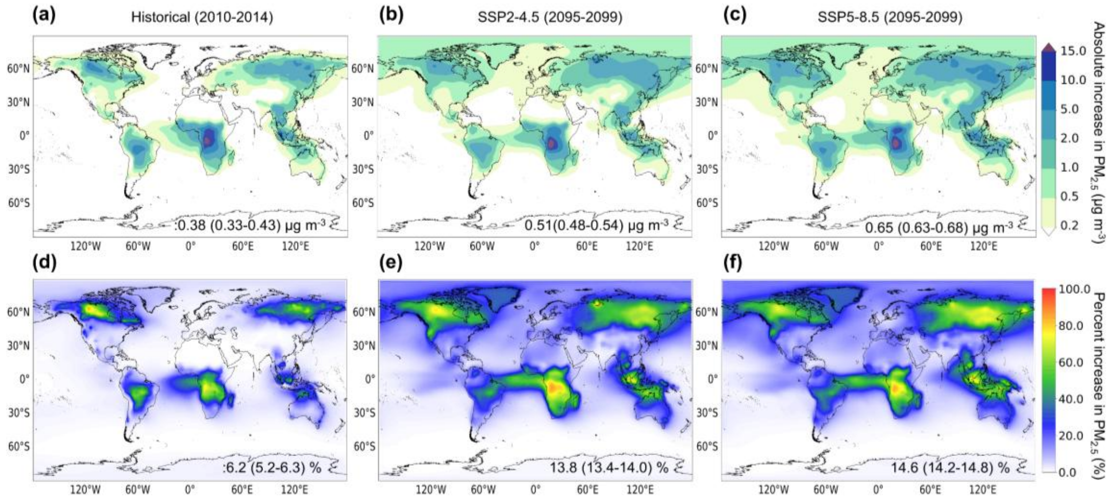

Supplementary Figure 12. Contribution of fire emissions to surface $PM_{2.5}$ concentrations during the historical period (2010 – 2014) and the late 21st century (2095–2099) under the SSP2-4.5 and SSP5-8.5 scenarios. (a) – (c) and (d)–(f) represent the absolute and relative contributions of fire emissions to annual mean surface-layer $PM_{2.5}$ concentrations, respectively.

Supplementary Table 1. Description of ESMs used in this study.

Name	Grid resolution	Land model	Description of fuel load calculation
CESM2[22] / CESM2-WACCM[22]	288 × 192 longitude/latitude	CLM5	These models track live leaf, stem, and root carbon pools, as well as intermediate transfer and storage carbon pools. All except live roots (i.e., leaves, stems, and litter) can be combusted when a fire occurs.
EC-Earth3-CC[23] / EC-Earth3-Veg[23]	512 × 256 longitude/latitude	HTESSEL and LPJ-GUESS v4	These models partition both live vegetation and litter carbon into branches, bark, trunks, leaves, and fine roots. All except fine roots (i.e., leaves, stems, and litter) are combusted when a fire occurs.

Supplementary Table 2. The information on climate factors datasets used in the ML framework, and other input parameters for future fire carbon emission projections.

Variable	Data source	Spatial resolution	Period
Fire carbon emissions	GFEDv4.1s[4]	0.25°×0.25°	2000–2014
	ESMs output	Dependent on model resolution	2000–2099
Burned area	GFEDv4.1s[4]	0.25°×0.25°	2000–2014
Climate factors: T2, RH, TP, W10, LAI, Evaporation	ERA5[5]	0.25°×0.25°	2000–2014
	ESMs output	Dependent on model resolution	2000–2099
Carbon mass in leaves, stems, and litter pool	ESMs output	Dependent on model resolution	2000–2099
Sampling times (Time)	Correspondence with input datasets		
Geographic coordinates (Coordinate)	Correspondence with input datasets		

Supplementary Table 3. Global total population for the age groups of 25+ and 65+ in the year 2010, and their respective values for the SSP2 and SSP5 scenarios in the year 2100 (billion) (numbers in parentheses represent the population of the 65+ age group in the sub-Saharan Africa region). Population data for the 2010 and future scenarios were obtained from the Gridded Population of the World version 4 (GPWv4) dataset (http://sedac.ciesin.columbia.edu/data/collection/gpw-v4/sets/browse) and SSP Public Database Version 2.0 (https://tntcat.iiasa.ac.at/SspDb/dsd?Action=htmlpage&page=30).

Age group	2010	SSP2-2100	SSP5-2100
25+	3.82	6.83	6.12
65+	0.54 (0.03)	2.67 (0.88)	3.26 (0.60)

Supplementary Table 4. **Global average importance of predictors for burned area in the SSP2-4.5 scenario (%).** The importance of each predictor was determined by calculating the proportion of the global absolute SHAP values averaged every five years among all predictors.

	W10	T2	RH	Evaporation	LAI	TP	Time	Coordinate
2000 – 2004	5.4	6.8	17.9	4.9	7.6	16.8	8.2	32.4
2005 – 2009	5.5	6.9	17.6	4.9	7.8	16.9	7.9	32.5
2010 – 2014	5.2	6.8	17.5	4.8	7.8	17.2	8.2	32.5
2015–2019	5.1	6.7	17.7	4.9	7.7	16.9	8.9	32.2
2020–2024	5.1	6.7	17.7	4.9	7.7	16.9	8.8	32.3
2025–2029	5.1	6.7	17.6	4.9	7.7	16.9	8.8	32.2
2030–2034	5.1	6.8	17.7	4.9	7.7	16.8	8.8	32.2
2035–2039	5.1	6.9	17.8	5.0	7.6	16.7	8.8	32.1
2040–2044	5.1	6.9	17.7	4.9	7.7	16.8	8.8	32.1
2045–2049	5.1	7.0	17.7	5.0	7.7	16.6	8.8	32.0
2050–2054	5.1	7.1	17.8	5.0	7.7	16.7	8.8	32.0
2055–2059	5.1	7.2	17.8	5.0	7.7	16.6	8.8	31.9
2060–2064	5.1	7.2	17.8	5.0	7.7	16.6	8.8	31.9
2065–2069	5.1	7.3	17.7	5.0	7.7	16.6	8.8	32.0
2070–2074	5.1	7.4	17.7	5.0	7.7	16.6	8.7	31.9
2075–2079	5.1	7.4	17.8	5.0	7.7	16.6	8.7	31.8
2080–2084	5.1	7.6	17.7	5.0	7.6	16.4	8.8	31.8
2085–2089	5.1	7.6	17.7	5.0	7.7	16.5	8.7	31.8
2090–2094	5.0	7.7	17.8	5.0	7.6	16.4	8.8	31.7
2095–2099	5.1	7.7	17.8	5.0	7.6	16.4	8.7	31.7

Supplementary Table 5. **Global average importance of predictors for burned area in the SSP5-8.5 scenario (%).** The importance of each predictor was determined by calculating the proportion of the global absolute SHAP values averaged every five years among all predictors.

	W10	T2	RH	Evaporation	LAI	TP	Time	Coordinate
2000 ﹣ 2004	5.4	6.8	17.9	4.9	7.6	16.8	8.2	32.4
2005 ﹣ 2009	5.5	6.9	17.6	4.9	7.8	16.9	7.9	32.5
2010 ﹣ 2014	5.2	6.8	17.5	4.8	7.8	17.2	8.2	32.5
2015–2019	5.1	6.7	17.6	4.9	7.7	16.9	8.9	32.2
2020–2024	5.1	6.7	17.6	4.9	7.6	16.9	8.8	32.2
2025–2029	5.1	6.8	17.7	4.9	7.6	16.9	8.9	32.1
2030–2034	5.1	6.8	17.6	4.9	7.7	16.9	8.8	32.1
2035–2039	5.1	7.0	17.6	5.0	7.7	16.8	8.9	32.0
2040–2044	5.1	7.1	17.7	5.0	7.6	16.7	8.9	31.9
2045–2049	5.1	7.2	17.8	5.0	7.6	16.7	8.8	31.8
2050–2054	5.1	7.5	17.7	5.0	7.7	16.5	8.9	31.7
2055–2059	5.1	7.6	17.7	5.0	7.7	16.5	8.8	31.7
2060–2064	5.1	7.8	17.7	5.0	7.7	16.3	8.8	31.6
2065–2069	5.1	8.0	17.7	5.0	7.7	16.2	8.8	31.4
2070–2074	5.1	8.3	17.8	5.1	7.8	16.0	8.7	31.3
2075–2079	5.1	8.4	17.8	5.0	7.8	16.0	8.7	31.2
2080–2084	5.1	8.8	17.7	5.0	7.8	15.8	8.7	31.0
2085–2089	5.1	9.1	17.7	5.0	7.8	15.7	8.7	30.9
2090–2094	5.1	9.3	17.7	5.0	7.9	15.6	8.6	30.7
2095–2099	5.1	9.6	17.8	5.1	7.9	15.4	8.6	30.6

References

1. Chen, T. & Guestrin, C. Xgboost: A scalable tree boosting system. *Proceedings of the 22nd acm sigkdd international conference on knowledge discovery and data mining*. 2016

2. Zhu, Q. et al. Building a machine learning surrogate model for wildfire activities within a global Earth system model. *Geosci. Model Dev.* **15**, 1899-1911 (2022).

3. Yu, Y. et al. Machine learning–based observation-constrained projections reveal elevated global socioeconomic risks from wildfire. *Nat. Commun.* **13**, 1–11 (2022).

4. van der Werf, G. R. et al. Global fire emissions estimates during 1997–2016. *Earth Syst. Sci. Data* **9**, 697–720 (2017).

5. Dee, D. P. et al. The ERA-Interim reanalysis: configuration and performance of the data assimilation system. *Q. J. R. Meteorol. Soc.* **137**, 553–597 (2011).

6. Gregor, L., Kok, S. & Monteiro, P. M. S. Empirical methods for the estimation of Southern Ocean CO_2: support vector and random forest regression. *Biogeosciences* **14**, 5551–5569 (2017).

7. Gade, K. A Non-singular Horizontal Position Representation. *J. Navigation* **63**, 395-417 (2010).

8. Zhao, J. et al. Improving Estimates of Dynamic Global Marine DMS and Implications for Aerosol Radiative Effect. *Journal of Geophysical Research: Atmospheres* **129**, e2023JD039314 (2024).

9. Wang, W. L. et al. Global ocean dimethyl sulfide climatology estimated from observations and an artificial neural network. *Biogeosciences* **17**, 5335–5354 (2020).

10. Randerson, J. T., Chen, Y., Van Der Werf, G., Rogers, B. & Morton, D. Global burned area and biomass burning emissions from small fires. *J. Geophys. Res. Biogeosci.* https://doi.org/10.1029/2012JG002128 (2012).

11. Xu, Z., Han, Y., Tam, C.-Y., Yang, Z.-L. & Fu, C. Bias-corrected CMIP6 global dataset for dynamical downscaling of the historical and future climate (1979–2100). *Sci. Data* **8**, 293 (2021).

12. Wu, C. et al. Reduced global fire activity due to human demography slows global warming by enhanced land carbon uptake. *Proc. Natl Acad. Sci. USA* **119**, e2101186119 (2022).

13. Terrer, C. et al. Nitrogen and phosphorus constrain the CO_2 fertilization of global plant biomass. *Nat. Clim. Change* **9**, 684–689 (2019).

14. Lundberg, S. M. & Lee, S.-I. A unified approach to interpreting model predictions. *Adv. Neural Inf. Process. Syst.* **30**, 4768–4777 (2017).

15. Senande-Rivera, M., Insua-Costa, D. & Miguez-Macho, G. Spatial and temporal expansion of global wildland fire activity in response to climate change. *Nat. Commun.* **13**, 1208 (2022).

16. Bey, I. et al. Global modeling of tropospheric chemistry with assimilated meteorology: model description and evaluation. *J. Geophys. Res. Atmos.* **106**, 23073–23095 (2001).

17. Gelaro, R. et al. The Modern-Era Retrospective Analysis for Research and Applications, version 2 (MERRA-2). *J. Clim.* **30**, 5419–5454 (2017).

18. Murray, L. T., Leibensperger, E. M., Orbe, C., Mickley, L. J. & Sulprizio, M. GCAP 2.0: a global 3-D chemical-transport model framework for past, present, and future climate scenarios. *Geosci. Model Dev.* **14**, 5789–5823 (2021)

19. Giles, D. M. et al. Advancements in the aerosol robotic network (AERONET) version 3 database-automated near-real-time quality control algorithm with improved cloud screening for

Sun photometer aerosol optical depth (AOD) measurements. *Atmos. Meas. Tech.* **12**, 169–209 (2019).

20. Saunois, M. et al. The Global Methane Budget 2000–2017. *Earth Syst. Sci. Data* **12**, 1561–1623 (2020).

21. Gurney, K. R. et al. Transcom 3 inversion intercomparison: model mean results for the estimation of seasonal carbon sources and sinks. *Global Biogeochem. Cycles* **18**, GB1010 (2004).

22. Danabasoglu, G. et al. The Community Earth System Model version 2 (CESM2). *J. Adv. Model. Earth Syst.* **12**, e2019MS001916 (2020).

23. Döscher, R. et al. The EC-Earth3 Earth system model for the Coupled Model Intercomparison Project 6. *Geosci. Model Dev.* **15**, 2973–3020 (2022).